

# Shedding new light on lipid biology with coherent anti-Stokes Raman scattering microscopy

Thuc T. Le,\* Shuhua Yue,\* and Ji-Xin Cheng<sup>1,\*†</sup>

Weldon School of Biomedical Engineering,\* Department of Chemistry,<sup>†</sup> Purdue University, West Lafayette, IN 47907

**Abstract** Despite the ubiquitous roles of lipids in biology, the detection of lipids has relied on invasive techniques, population measurements, or nonspecific labeling. Such difficulties can be circumvented by a label-free imaging technique known as coherent anti-Stokes Raman (CARS) microscopy, which is capable of chemically selective, highly sensitive, and high-speed imaging of lipid-rich structures with submicron three-dimensional spatial resolution. We review the broad applications of CARS microscopy to studies of lipid biology in cell cultures, tissue biopsies, and model organisms. Recent technical advances, limitations of the technique, and perspectives are discussed.—Le, T. T., S. Yue, and J.-X. Cheng. *Shedding new light on lipid biology with coherent anti-Stokes Raman scattering microscopy*. *J. Lipid Res.* 2010. 51: 3091–3102.

**Supplementary key words** adipocytes • atherosclerosis • cancer • lipase/hepatic • lipid kinases • lysophospholipid • nutrition

Lipids play a critical role in human health and diseases. Phospholipids, glycolipids, and sterol lipids are the major components of the cell membrane (1). Sphingolipids constitute up to 80% of the myelin sheaths, which are the membranous structures that wrap around the axons for insulation and for proper propagation of electrical impulses (2). Glycerolipids or triglycerides serve as the cytoplasmic energy depots (3). Bioactive lipids including sphingolipid second messengers, second messengers from phosphatidylinositol, lipid activators of G-protein coupled receptors, and lipid activators of nuclear receptors regulate a wide range of biological processes including cell death, cell proliferation, senescence, migration, and inflammation (4, 5). Dysregulation of lipid metabolism in hyperlipidemia or obesity can lead to many debilitating diseases including diabetes, atherosclerosis, and neurodegenerative diseases (6, 7).

Despite the ubiquitous roles of lipids in biology, the detection of lipids has relied on invasive techniques and population measurements. The molecular profiles of the lipid-rich structures are evaluated by measurements of total lipid extracts with liquid or gas chromatography coupled to mass spectrometry (8). This approach is inexact because it measures lipid molecules from areas other than the structures of interest. Furthermore, spatial information, which is critical to understanding the function of lipids (9), is inaccessible with the bulk measurement techniques. To visualize the lipid-rich structures, fluorescently tagged lipid molecules, which intercalate with the lipid-rich structures, are used (10, 11). Nevertheless, the use of the fluorescent lipid molecules to label lipid-rich structures is problematic for several reasons. First, to facilitate the transport of the fluorescent lipid molecules into cells, cell fixation procedures are often performed (12). This procedure prevents monitoring the dynamic responses of lipid-rich structures to stimuli or the disease processes. Second, labeling efficiency is highly dependent on the type of fluorescent lipid molecules (12), thus posing a significant problem to the quantitation of lipid-rich structures. Third, the intercalation of fluorescent lipid molecules can lead to changes in the properties of lipid-rich structures. For instance, incorporation of fluorescent lipid molecules into the cell membrane can induce membrane phase separation and membrane microdomain formation, which can perturb critical cellular processes including signal transduction and endocytosis (13).

As an alternative to fluorescence, signals from molecular vibration provide an attractive means for label-free chemical imaging. In particular, Raman scattering has been widely used for spectroscopic study of biomolecules (14). The Raman-scattered photons exhibit frequency

Abbreviations: CARS, coherent anti-Stokes Raman scattering; E-CARS, epi-detected CARS; F-CARS, forward-detected CARS; IR, infrared; IVUS, intravenous ultrasound; LD, lipid droplet; NA, numerical aperture; NLO, nonlinear optical; ps, picosecond; SHG, second harmonic generation; SRS, stimulated Raman scattering; TPEF, two-photon excited fluorescence.

<sup>†</sup>To whom correspondence should be addressed.  
e-mail: jcheng@purdue.edu

This work is supported by a Ruth L. Kirschstein NRSA postdoctoral fellowship F32HL089074 to T.T.L. and R01EB007243 and a Showalter grant to J.-X.C.

Manuscript received 2 June 2010 and in revised form 16 August 2010.

Published, JLR Papers in Press, August 16, 2010  
DOI 10.1194/jlr.R008730

shifts associated with the molecular vibration and give rise to a Raman spectrum specific to the molecule. Because each molecule has its unique Raman signature, Raman scattering has been widely employed to study the intrinsic chemical composition of biological structures without the need for labeling (15–17). However, the applications of Raman scattering to biological imaging are faced with many technical challenges. Following light-matter interaction, approximately one in ten million photons undergoes Raman scattering. The spontaneous Raman cross-section is  $\sim 10^{-30}$  cm<sup>2</sup> per molecule as compared with the fluorescence cross-section of  $\sim 10^{-16}$  cm<sup>2</sup> per molecule (15). Weak Raman signal requires long integration time of  $\sim 100$  millisecond per pixel for image acquisition, or hours for an image of 512 by 512 pixels. This timescale is unsuitable for imaging dynamic living biological systems. In addition, autofluorescence intrinsic to many biological structures at visible wavelength is stronger than Raman scattering. In such cases, informative Raman spectral details are masked by the fluorescence.

Fortunately, the Raman scattering signal can be enhanced by several orders of magnitude with a nonlinear optical (NLO) method called coherent anti-Stokes Raman scattering (CARS) microscopy (18). CARS is a four-wave mixing process in which three laser fields at the pump ( $\omega_p$ ), Stokes ( $\omega_s$ ), and probe ( $\omega'_p$ ) frequencies interact with a medium to generate a new field at the anti-Stokes frequency  $\omega_{as} = (\omega_p - \omega_s) + \omega'_p$ . In most experiments, the pump field and probe field come from the same laser beam. CARS signal arises from any medium with nonzero third-order susceptibility (19). The signal is enhanced when the beating frequency ( $\omega_p - \omega_s$ ) is in resonance with a molecular vibration frequency, which provides the vibrational contrast in a CARS image. Owing to the coherent addition of the CARS radiations, the CARS intensity is quadratically dependent on the number of the vibrational oscillators in the focal volume. In the samples with high concentration of vibrational oscillators, CARS signal is many folds stronger than spontaneous Raman scattering signal, which is linearly dependent on the number of vibrational oscillators. The large signal level in CARS microscopy enables high-speed imaging, which is important for live cell and tissue studies. By scanning the lasers of high repetition rate (in MHz), an image acquisition speed at one frame per second has been achieved (20) and has been recently increased to twenty frames per second (21). The high imaging speed not only avoids respiration-induced image distortion during *in vivo* imaging, but also allows real-time inspection of biological processes. Moreover, the NLO excitation ensures that the CARS signal is only generated at the center of the focus, offering CARS microscopy an inherent 3-D spatial resolution. The lateral and axial resolutions with a 60 $\times$  water immersion objective were measured to be 0.23 and 0.75  $\mu$ m (22), which allows detection of subcellular structures in a tissue environment.

With the developments of CARS imaging platforms, high-speed three-dimensional chemical imaging of living

biological systems has been widely demonstrated (23–25). Most importantly, with the beating frequency ( $\omega_p - \omega_s$ ) tuned to c.a. 2845 cm<sup>-1</sup> that matches the symmetric stretch vibration of CH<sub>2</sub> groups, a strong CARS signal is produced from lipid-rich structures that are abundant in CH<sub>2</sub> groups. With such capability, CARS microscopy has found broad applications in the field of lipid biology in recent years (26, 27). In this review, we describe the basic principle of CARS microscopy and its recent development to biologists who are unfamiliar with CARS technology. Successful applications of CARS microscopy to the studies of lipids in health and diseases are summarized and discussed. In particular, we highlight the innovative studies of two important lipid-rich structures, cytoplasmic lipid droplets and axonal myelin sheath.

## HISTORY OF DEVELOPMENT

The phenomenon of coherent Raman scattering was first reported by scientists at the Ford Motor Co. in 1965 (28). Since the introduction in the early 1970s (29), CARS spectroscopy has been widely used as a spectroscopic tool (30). The first application of CARS to imaging was demonstrated in 1982 with a noncollinear beam geometry by scientists at the Naval Research Laboratory (31). Nearly two decades later, CARS microscopy was revisited with a collinear beam configuration at the Pacific Northwest National Laboratory in 1999 (32). Since then, the CARS renaissance has stimulated further development and applications by researchers from broad scientific disciplines. Continuous contributions from many research groups over the last decade have vastly improved the design, stability, and sensitivity of CARS microscopy [for reviews, see (18, 23–25)].

## ESSENTIAL FEATURES OF A HIGH-SPEED CARS MICROSCOPE

In this section we describe a high-speed, multifunctional CARS microscope (**Fig. 1**) that is ready for biological applications. This platform results from theoretical study (22) and multi-step technical advances (18, 25) of CARS microscopy. Important features of the microscope are described in the sections below.

### Near IR laser excitation

The near IR lasers avoid two-photon electronic enhancement of the nonresonant background (32), reduce the photodamage induced by multiphoton absorption (33), and diminish tissue scattering leading to increased optical penetration depth (34). As a two-beam modality, CARS microscopy is mostly operated with picosecond (ps) pulses, either from two synchronized Ti:sapphire lasers (35) or from a synchronously pumped Optical Parametric Oscillator system (34). Picosecond pulse excitation not only provides sufficient spectral resolution (36) but also increases the ratio of resonant signal to nonresonant background (35). Although tunable ps laser

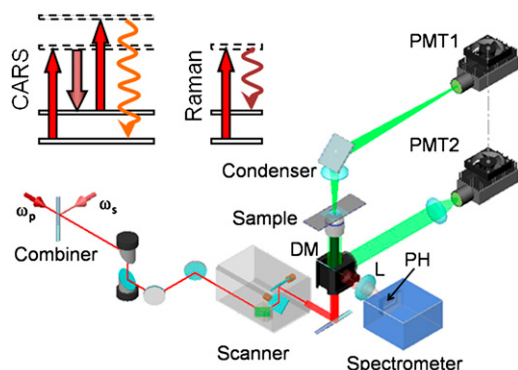


**Fig. 1.** A high-speed CARS microscope for lipid research. Pump and Stokes laser beams are collinearly combined, directed into a laser scanning box, and focused into the samples. Emitted photons are collected by a condenser for forward-detected CARS (F-CARS) or by the focusing objective for epi-detected CARS (E-CARS). PMT1 and PMT2 are detectors for F-CARS and E-CARS, respectively. The pump laser is also used for generating spontaneous Raman signals from an object visualized by CARS. A spectrometer with a pinhole attached to the side port of the microscope is used for confocal recording of spontaneous Raman spectra. Although not shown, sum frequency generation (SFG) and two-photon excited fluorescence (TPEF) imaging can be performed on the same platform. PH, pinhole; DM, dichroic mirror; L, lens; PMT, photomultiplier tube.

systems operating in the near IR range are widely accepted for high-speed CARS imaging [for reviews, see (18, 23, 25)], the reduced efficiency of NLO process caused by longer pulse duration (37) hinders wide application of ps lasers to two-photon excited fluorescence (TPEF) and second harmonic generation (SHG) imaging. Therefore, toward the goal of coupling the CARS imaging modality to other widely used platforms of multiphoton microscopy, Pegoraro et al. (38) and Chen et al. (39) showed independently high-speed CARS imaging of lipids with femtosecond (fs) laser pulses. Commercial CARS microscopes with either ps or fs laser sources are now available through Leica and Olympus, respectively.

### Collinear beam geometry

Non-collinear beam geometry was used in CARS spectroscopy to fulfill the phase matching condition (30). When the interaction length became very small ( $\sim 1 \mu\text{m}$ ) under the tight focusing condition in microscopy, the phase matching condition was fulfilled with a collinear beam geometry for forward-detected CARS (F-CARS) (32). The collinear beam geometry greatly simplified the optical alignment and has been a key step in producing high-quality CARS images.

### Forward-detection versus epi- (i.e., backward-) detection

For objects that are comparable or larger than the wavelengths of incident lasers, the CARS signal goes forward as a result of constructive addition of radiations (18). Importantly, because the CARS signal is highly directional in the forward direction, an air condenser is sufficient for collection of the F-CARS signal. F-CARS is suitable for imaging

lipid bodies or myelin sheath in cultured cells or sliced tissues (40, 41). For objects with an axial length much smaller than the excitation wavelengths, the phase matching condition is fulfilled in both forward and backward directions, which constitute the first mechanism for epi-detected CARS (E-CARS) (42). E-CARS also arises from the discontinuity of  $\chi^{(3)}$  at an interface (22) and back-scattering of forward CARS photons (21). E-CARS is important for live animal imaging where the epi-detected signal arises from backscattering of the forward propagating CARS photons by the tissue (21, 43).

### Laser-scanning on a confocal microscope platform

The most significant advantage of CARS over spontaneous Raman is its large signal level to allow for high-speed vibrational imaging. This advantage has been realized by scanning pulsed lasers of high repetition rates (in MHz), which resulted in an image acquisition speed of a frame per second (20). Video rate imaging can be realized by scanning the laser with a polygon mirror or a resonant scanner (21, 44).

### Multimodal NLO imaging

An important advantage of the CARS microscope is that other NLO modalities, including TPEF and SFG, can be implemented on the same platform. Multimodality is important because different NLO imaging methods have their distinctive advantages: TPEF can be used to visualize proteins and ions with fluorescent labeling or specific autofluorescent structures; SFG is selective to noncentrosymmetric molecular assemblies, such as collagen fibrils and crystals; and CARS is naturally sensitive to lipid-rich structures such as adipocytes. The pulsed laser beams for CARS could be simultaneously used for TPEF and electronic SFG imaging. For instance, Fu et al. (45) demonstrated multimodal NLO imaging of ex vivo spinal tissues by CARS imaging of myelin sheath, SFG imaging of astrocyte processes, and TPEF imaging of calcium indicators on the same platform. Technically, one can separate the CARS and TPEF signals based on their spectral and coherence properties. The CARS photons are highly directional in the forward and can be collected with an air condenser of low numerical aperture (NA). The fluorescence is spectrally broad and incoherent; it is therefore negligible after the narrow bandpass CARS filters and the air condenser in the forward channel. Due to the Gouy phase shift, the forward SFG signal is deflected from the optical axis (46) and is fairly weak if a low-NA air condenser is used. Instead, the backward SFG and TPEF photons can be effectively collected by the high NA laser-focusing objective. Examples of CARS-based multimodal NLO imaging of lipid-rich structures are shown in **Fig. 2**.

### Coupling CARS imaging with spontaneous Raman spectroscopy

It has been realized that the CARS and spontaneous Raman have their distinctive advantages; CARS permits

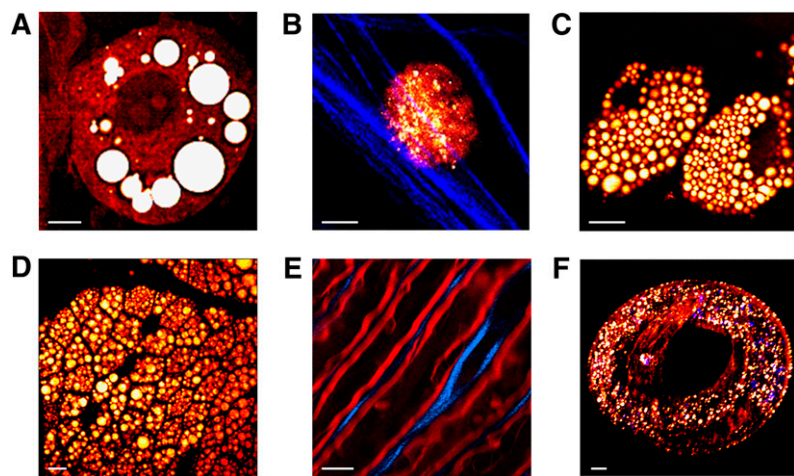


**Fig. 2.** CARS-based multimodal NLO imaging of lipid-rich structures. A: CARS image of a differentiating 3T3-L1 cell. B: Overlaid CARS and SFG image of a lipid-rich tumor cell (red) on collagen fibrils (blue). C: CARS image of two lipid-rich foam cells. D: CARS image of lipid-rich intestinal cells of a C57BL/6J mouse after feeding. E: Overlaid CARS and SFG image of myelin sheaths (red) and astroglial processes (blue). Image is a courtesy of Terry B. Huff. F: Overlaid CARS and TPEF image of neutral lipid droplets (red) and autofluorescent lipid species (blue) in a living *C. elegans*. Scale bars: 5  $\mu\text{m}$ . Images adapted from references (48, 59, 90, 98).

high-speed imaging by focusing the energy on a single Raman band whereas spontaneous Raman permits complete fingerprint analysis at a pixel of interest. Recently, a compound Raman microscope has been demonstrated by using the same ps laser source for high-speed coherent Raman imaging of a sample and confocal Raman spectral analysis of lipid-rich structures such as sebaceous gland (47) and fat in *Caenorhabditis elegans* (48). Examples of CARS imaging and Raman spectral analysis of lipid-rich structures are shown in Fig. 3.

## APPLICATIONS OF CARS MICROSCOPY TO LIPID BIOLOGY

### Study of lipid droplet biology

Lipid droplets (LDs) have been well observed as a prominent cytoplasmic structure (49). However, the studies of LDs have been hindered by a long held perception of LDs as inert energy depots. Contrary to this perception, increasing evidence points to an active role of LDs in biological processes (50). In addition to storing triglycerides

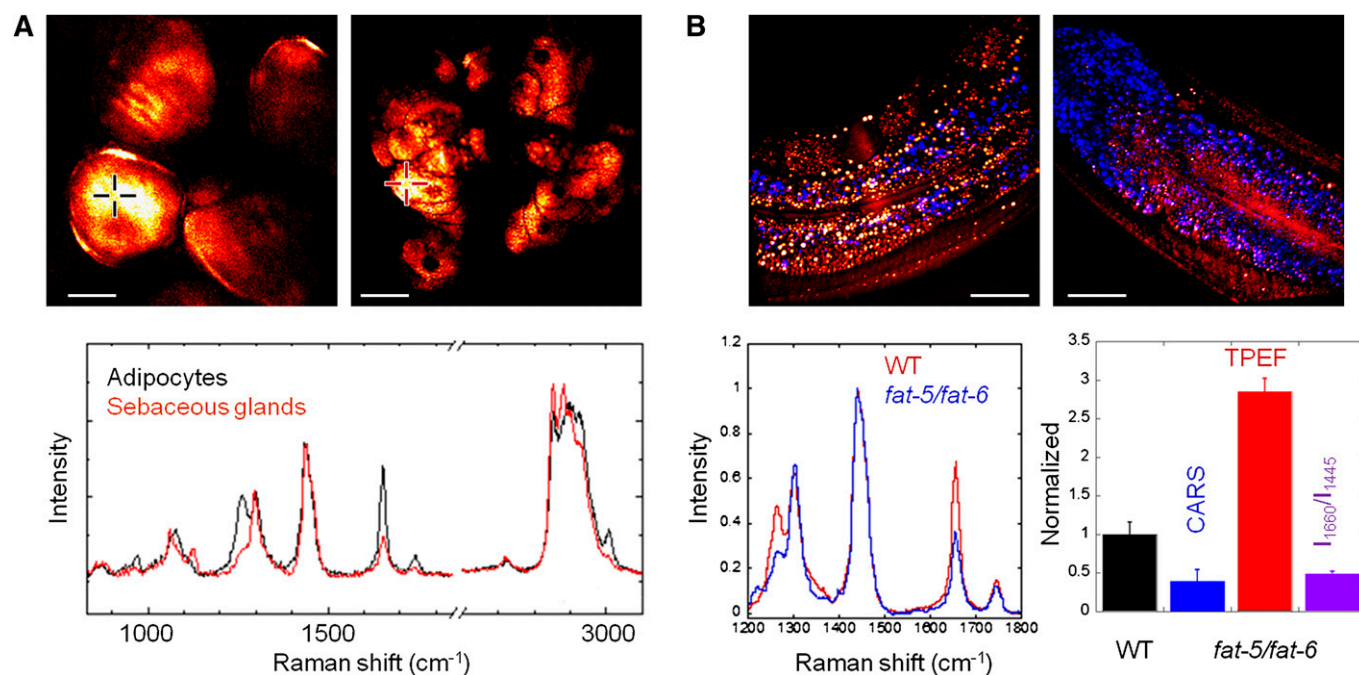


**Fig. 3.** CARS imaging and quantitative analysis of lipid expression and composition. A: CARS images of subcutaneous adipocytes (upper left panel) and sebaceous glands (upper right panel) in the ear of a living Balb/c mouse. The cross-hairs mark the locations for spontaneous Raman spectra acquisition. The bottom graph presents overlaid Raman spectra of subcutaneous adipocytes (black) and sebaceous glands (red). B: Overlaid CARS and TPEF images of neutral lipids (red) and autofluorescent lipids (blue) in a wild-type (upper left panel) and a *fat-5/fat-6* double mutant (upper right panel) *C. elegans*. The *fat-5/fat-6* double mutant has genetic deletions of palmitoyl-CoA desaturase *fat-5* and stearoyl-CoA desaturases *fat-6*. Lower left panel: Overlaid Raman spectra of neutral lipids in wild-type (red) and *fat-5/fat-6* double mutant (blue) *C. elegans*. Lower right panel: Quantitative comparison of the expression level of neutral (blue) and autofluorescent (red) lipids and the lipid-chain unsaturation (purple) between wild-type (black) and *fat-5/fat-6* double mutant *C. elegans*. The quantitative values are normalized to one for wild-type and comparatively for *fat-5/fat-6* double mutant *C. elegans*. The lipid-chain unsaturation is measured by the I1660/I1445 ratio in Raman spectra. Scale bars: 25  $\mu\text{m}$ . Images adapted from references (47, 48).

for energy, LDs also store phospholipids and sterols, which are critical for the growth and maintenance of the cell membrane (51). Increased cytoplasmic LD accumulation is proposed to be a mechanism to avoid apoptosis when cells are exposed to excess unesterified fatty acids (52). The observation of LD interaction with cellular organelles such as the endoplasmic reticulum, mitochondria, and endosomes suggests that LDs might facilitate intracellular lipid transport (53). Interestingly, LDs might play a role in mediating host-pathogen interaction because LD accumulation increases upon hepatitis C viral infection and the replication of hepatitis C virus interacts with LDs (54). Most significantly, excess accumulation of cytoplasmic LDs is strongly associated with major diseases including obesity, type II diabetes, hepatic steatosis, and atherosclerosis (3).

The emerging dynamic view of LDs is attracting biologists to study the biology of LDs. In particular, the discoveries of LD-associated perilipin, adipophilin, and TIP47 (PAT) proteins, Rab18, DGAT2, and caveolin are posing questions about how LDs are formed, grown, and mobilized (55). More than ever, the ability to monitor LDs in real time is critically needed. With the capability of label-free visualization of LDs, CARS microscopy is highly suitable for the studies of LD dynamics. Moreover, green fluorescent protein and red fluorescent protein-tagged proteins that associate with LDs have been made available (56). Simultaneous CARS imaging of LDs and TPEF imaging of GFP and RFP-tagged proteins would allow the dynamic correlation between protein localization and LD formation, growth, or mobilization in living cells.

The application of CARS microscopy to the studies of LD biology is slowly gaining traction. Using CARS microscopy, Nan et al. (40) observed that the formation of large LDs in 3T3-L1 cells was preceded by the initial clearance of small LDs after adipogenesis induction. By simultaneous CARS imaging of LDs and TPEF imaging of labeled mitochondria, Nan et al. (57) further revealed possible interaction between LDs and cellular organelles in adrenal cortical Y-1 cells. Yamaguchi et al. (58) used CARS imaging to examine lipolysis of LDs and found a possible role of CGI-58 protein in the vesiculation of small LDs from large LDs. Le et al. (59) used CARS imaging to examine the phenotypic variability in LDs accumulation among clonal cells and found that variability in LD formation is the consequence of the ability of cells to process insulin. By simultaneous TPEF imaging of viral RNA distribution and CARS imaging of LDs, Lyn et al. (60) found that lipid metabolism inhibitors can cause disruption of hepatitis C viral replication. These initial studies showcase possible applications of CARS microscopy. However, the full impact of CARS microscopy on LD biology is still dependent on further in-depth studies and broader utilization of CARS imaging capability.

#### Study of lipid metabolism in *C. elegans*

The pathways of lipid metabolism are highly conserved from *C. elegans* to human (61, 62). Being optically transparent and having highly tractable genetics, *C. elegans* has

been serving as a model organism to study the pathogenesis of metabolic diseases (61). In *C. elegans*, lipids are stored in the form of LDs mostly in the intestinal cells and to some extent in the hypodermal cells (63). A wide range of lipid synthesis enzymes, including desaturases and elongases, are present in *C. elegans*, which account for a full range of saturated, monounsaturated, and polyunsaturated fatty acids of various lengths (63). Genetic deletions of the lipid synthesis enzymes generally lead to quantifiable phenotypes, including changes in the quantity and composition of lipids, stunted growth, altered movement, reduced body size, defective neurotransmission, and shortened lifespan (64, 65). Therefore, *C. elegans* is a desirable model for the integrative studies of how a specific lipid synthesis enzyme impacts the physiology, metabolism, and behavior of an organism.

However, the studies of lipid metabolism in *C. elegans* are hindered by several technical challenges. First, the labeling efficiency of LDs in *C. elegans* can vary from worm to worm. Labeling efficiency is also lower in live worms than in fixed worms (66). In addition, LDs of the intestinal cells are labeled but not LDs of the hypodermal cells (67). Thus, visualization and quantitation of LDs in *C. elegans* are subject to large technical errors. Second, the fluorescent spectra of labeling dyes overlap with the fluorescent spectrum of autofluorescent particles. The expression of autofluorescent particles in *C. elegans* is strongly correlated to oxidative stress and aging (68, 69). Thus, the studies of LDs with labeling mask information, which could be critical to the evaluation of *C. elegans* physiology. Third, the analysis of LD composition is currently performed using gas chromatography (70). This measurement approach provides a population average value and masks the individual variability intrinsic to worms. Furthermore, the dynamic correlation between lipid composition and *C. elegans* behavior is not possible with bulk measurement techniques.

CARS microscopy presents an unprecedented opportunity to study lipid metabolism in living *C. elegans*. In the first application of CARS microscopy to *C. elegans*, Hellerer et al. (67) monitored changes in the lipid packing state of LDs as a function of larvae developmental stages. Hellerer et al. also examined lipid storage in wild-type and mutants of *C. elegans* with genetic deletions of proteins involved in the feeding behavior and insulin signaling pathway. In another study, Morck et al. (71) used CARS microscopy to evaluate the impact of cholesterol lowering drugs on lipid storage in *C. elegans*. This study shows that statin treatment reduces the level of Nile Red staining, but does not affect neutral lipid storage in *C. elegans* as detected with CARS microscopy. In a separate study, it was found that Nile Red stains a subset of gut granules, which does not correlate with lipid content (72). Collectively, these studies suggest that Nile Red staining might not be a reliable measure of lipid content in *C. elegans*. Most recently, Le et al. (48) identified coexisting neutral and autofluorescent lipid species with simultaneous CARS and TPEF imaging (Fig. 3B). Fingerprint spectral analysis using confocal Raman microspectroscopy on the same platform provides the

capability of detecting lipid chain unsaturation. Le et al. also measured lipid-chain unsaturation of single LDs in *C. elegans* with genetic deletions of genes encoding for  $\Delta 9$  desaturases (Fig. 3B). These results highlight the capability of CARS imaging combined with spontaneous Raman microspectroscopy for analysis of complex genotype-phenotype relationships between lipid storage, peroxidation, and desaturation in single living *C. elegans*. Together, these initial studies showcase the versatility of CARS microscopy for noninvasive and label-free visualization and compositional analysis of LDs in *C. elegans*. When combined with recent advances in *C. elegans* genetics (73) and high-throughput screening (74), CARS microscopy is expected to facilitate rapid functional studies of lipid metabolism at the genomic scale and advance our understanding of the roles of lipids in human health and diseases.

### Detection of atherosclerosis by CARS-based multimodal microscopy

Atherosclerosis is a complex process that begins in early adolescence and progressively develops over time. Nonetheless, the first diagnosis of atherosclerotic plaques is normally when a heart attack occurs. Existing diagnostic tools for atherosclerosis are limited and inadequate for early detection. Noninvasive testing of atherosclerosis such as the cardiac stress test yields a positive diagnosis only when the lumen narrowing is at 75% or greater. Anatomical diagnosis including computed tomography, magnetic resonance imaging, and intravenous ultrasound (IVUS) are expensive and not widely prescribed and can detect only advanced calcified plaques (75). In addition, complications from atherosclerosis are not only dependent on stenosis or lumen occlusion but also on the rupture of vulnerable plaques. Thus, a diagnosis of atherosclerotic plaques should include both anatomical features for stenosis evaluation and molecular composition for vulnerability evaluation (76, 77). However, the capability of existing diagnostic tools for atherosclerosis is insufficient to satisfy this requirement.

Several recent studies highlight the capability of CARS-based multimodal NLO microscopy for plaque detection and molecular composition analysis. Le et al. (78) and Wang et al. (79) employed multimodal NLO microscopy to visualize the composition of arterial walls and atherosclerotic plaques. They demonstrated label-free visualization of elastin, collagen fibrils, smooth muscle cells, endothelial cells, foam cells, and extracellular lipid deposits using combined TPEF, SHG/SFG, and CARS imaging modalities. Le et al. showed that a plaque can be detected with multimodal NLO imaging by several ways. First, SHG imaging revealed that the arrangement of collagen fibrils is parallel with each other in healthy arterial walls but disorganized in plaques. Second, measured from the lumen, TPEF signal from elastin appears before SHG signal of collagen fibrils in healthy arterial walls, whereas in the plaque areas, SHG signal appears together with TPEF signal because collagen fibrils breach the internal elastic lamina and grow into the lumen. Thus, the order of appearance of TPEF and SHG signal can indicate the plaque location.

Third, a plaque can also be identified by CARS visualization of lipid-rich foam cell and extracellular lipid deposits. Hence, Le et al. suggest that multimodal imaging can significantly improve the sensitivity and accuracy of plaque detection. In a different study, Wang et al. (80) further used multimodal NLO microscopy to identify different atherosclerotic types as classified by the American Heart Association Committee. More recently, Lim et al. (81) employed multimodal NLO microscopy to evaluate the impact of a high-fat and high-cholesterol diet on the composition of atherosclerotic plaques in ApoE<sup>-/-</sup> mice. Kim et al. (82) employed multiplex CARS microscopy to describe the changes in the chemical profiles of atherosclerotic lipids in response to statin drug treatment using the ApoE<sup>-/-</sup> mice model. Ko et al. (83) explored the capability of multimodal imaging to visualize atherosclerotic plaque development in myocardial infarction-prone rabbits. Together, these studies show a growing interest in the applications of CARS microscopy to the studies of atherosclerotic lesions in animal models.

However, clinical application of CARS imaging for early detection of plaques is dependent on the successful development of CARS endoscopy. Currently, the tissue penetration depth of CARS microscopy is c.a. 100 microns. This penetration depth is insufficient for visualization of arterial lumen from the adventitia. In addition, connective and fatty tissues surrounding the artery would scatter light and reduce the visibility of CARS imaging. Therefore, effective deployment of CARS imaging should be done from the arterial lumen. This deployment requires CARS endoscopy, where the delivery of the excitation laser and collection of emitted signal are accomplished using flexible fiber optics, miniaturized objective, and scan heads (84, 85). Ideally, CARS endoscopy should be deployed on a catheter bundle that is also capable of optical coherent tomography and IVUS (75). This combinatorial scheme would allow both anatomical mapping of plaques with optical coherent tomography and IVUS and compositional analysis with CARS/SHG/TPEF. Although CARS endoscopy has yet to be realized, recent advances in NLO endoscopy (86) suggest its eventual reality. The potential benefits of CARS endoscopy for the detection and diagnosis of atherosclerotic plaques should encourage future research and development on this front.

### CARS imaging of intestinal lipid absorption

Obesity is an established risk factor for major human diseases including cancer, diabetes, and cardiovascular diseases (6). The prevalence of obesity in developed countries poses a significant challenge to global health management. Obesity is the consequence of the imbalance between energy intake and expenditure. To manage obesity, several approaches have been taken including diet modification, exercise regiment, bariatric surgery (87), and intestinal sleeve implantation (88). Although diet and exercise are the most widely accepted recommendation to combat obesity, many people still struggle to reduce their body weight with this approach. Alternatively, bariatric surgery and intestinal sleeve implantation have shown

significant reduction of body weight and improvement in the glycemic index. Nonetheless, the long-term effects of surgery and implantation have yet to be determined. Another approach to combat obesity is through pharmaceutical intervention. However, this approach requires in-depth understanding of an individual's metabolic activity, energy homeostasis, genetics, molecular control of adipogenesis, neuronal control of satiety, and other characteristics to design effective drugs with minimal side effects.

An effective approach to restoring the energy balance is to minimize the energy intake by controlling the absorption of dietary lipids (89). Toward this goal, researchers have studied key aspects of lipid emulsification, hydrolysis, uptake into enterocytes, intracellular trafficking, storage, and secretion into the circulation. However, tracking the movement of dietary lipids relies on histology and electron microscopy for visualization and bulk measurements for quantitative lipid analysis. These methods provide static snapshots of intestinal lipid absorption but leave the dynamic process largely to extrapolation.

Recently, Zhu et al. (90) described the first use of CARS microscopy for real-time visualization of lipid absorption by the small intestine in living mice. With minimally invasive surgery, Zhu et al. monitored the enterocytes as a function of time after feeding and found a dynamic cytoplasmic triacylglycerol pool (Fig. 4A). Especially, Zhu et al. found that acyl CoA:diacylglycerol acyltransferase 1 (DGAT-1) deficient mice exhibited higher level of cytoplasmic triacylglycerol storage compared with wild-type mice. Previous studies showed that DGAT-1 deficient (*Dgat1*<sup>-/-</sup>) mice were resistant to diet-induced obesity and

had improved insulin sensitivity and decreased tissue levels of triacylglycerol compared with wild-type mice. Thus, DGAT-1 was suggested to be a pharmaceutical target for the treatment of human obesity and diabetes (91). However, the mechanism underlying the protective effect of DGAT-1 was not clearly understood. To study the roles of DGAT-1, Lee et al. (92) restored the expression of DGAT-1 protein only in the intestine (*Dgat1*<sup>IntONLY</sup>) of *Dgat1*<sup>-/-</sup> mice. *Dgat1*<sup>IntONLY</sup> mice were not resistant to high-fat diet-induced hepatic steatosis or obesity despite the absence of DGAT-1 protein in the liver and adipose tissues. This study suggests a role of DGAT-1 in regulating dietary fat secretion out of enterocytes, thus affecting the level of dietary fat in tissues. Together, these initial studies demonstrate the use of CARS imaging to study the role of the DGAT-1 enzyme in intestinal lipid absorption. Future applications of CARS imaging should allow functional studies of other enzymes in intestinal lipid absorption or evaluation of drugs aiming at interfering with the energy intake to treat obesity and diabetes.

### Study of lipids in cancer development

Intracellular lipid bodies have been observed in many types of cancers (93, 94). Early clinical studies in the 1970s linked lipid-rich carcinoma of mammary glands to high incidence of cancer mortality, metastatic tumors, and aggressive clinical behaviors (93, 95). More recently, increased expression of lipid metabolism genes are found in aggressive brain, mammary, and prostate cancer (96, 97). These observations suggest a link between lipid metabolism and cancer aggressiveness. Nonetheless, lipid metabolism has not been used as a prognosis factor for cancer aggressiveness due to the lack of a mechanistic understanding.

Using CARS microscopy, Le et al. (98) examined the impacts of excess lipids on cancer development. In a Balb/c mice lung cancer model, Le et al. reported that excess lipids due to diet-induced hyperlipidemia and increased visceral adiposity strongly correlate with increased cancer metastasis. In tissue cultures, Le et al. found that excess lipids caused perturbations to cancer cell membrane, induced cytoplasmic lipid accumulation, and promoted cancer invasiveness. The presence of cytoplasmic lipid bodies allowed CARS visualization of migrating cancer cells on collagen fibers and circulating tumor cells in blood samples. In recent years, CARS flow cytometry has been successfully applied to characterize lipid-rich cells and particles in microfluidic chambers (99, 100). The observation of lipid-rich circulating tumor cells suggests possible development of label-free intravital CARS flow cytometry for clinical cancer diagnosis.

In addition to the direct impacts on cancer cells, Le et al. (101) reported perturbation by excess lipids on tumor microenvironments. Using a Sprague-Dawley rat mammary cancer model, Le et al. examined the composition of the mammary tumor microenvironment and found larger lipid droplets of adipocytes and higher density of collagen fibrils in diet-induced obese rats as compared with lean rats. Given the known roles of adipocytes in supporting tumor growth (102) and collagen fibrils in supporting

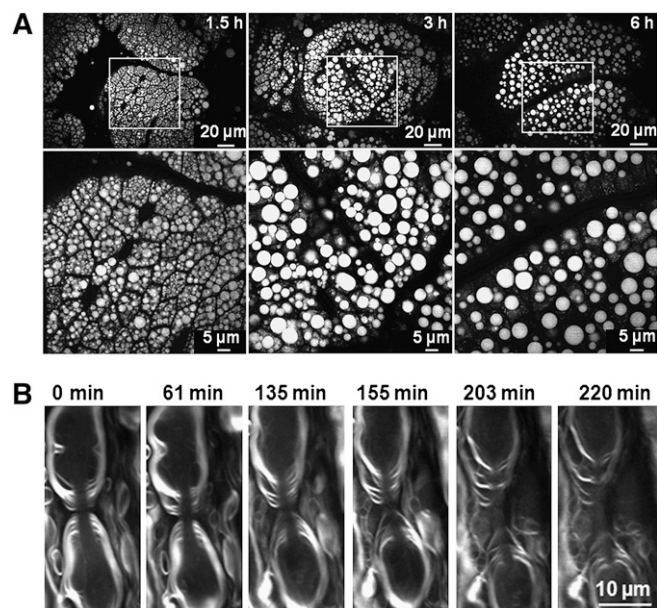


**Fig. 4.** Imaging the dynamics of biological processes with CARS microscopy. A: CARS imaging of the intestinal villi of a C57BL/6J mouse at 1.5 h, 3 h, and 6 h after feeding. Images are of different villi at different time points. B: CARS imaging of paranodal myelin splitting and retraction induced by 1 mM glutamate in the explanted spinal cord white matter of a Long-Evans rat. Images adapted from references (90, 112).

cancer cell migration (103, 104), this observation suggests that excess lipids promote a tumor microenvironment conducive to tumor growth and metastasis.

To satisfy the high proliferation rate, a cancer cell needs to increase its biomass by increasing its uptake of nutrients including glucose and lipids (105, 106). However, as many lipid molecules participate in cell signaling (4), it is conceivable that they also influence cancer cell behaviors. Future studies that focus on profiling the lipid composition and the behavior of cancer cells could lead to a better understanding of the roles of lipids in cancer. With the capability for label-free visualization and noninvasive compositional analysis of lipids, CARS microscopy is an invaluable tool to the studies of lipids in cancer development.

### Study of skin biology

Skin plays an important role in human physiology by providing a protective barrier against germs, an insulation layer against fluctuating temperatures, and a sensory organ for heat, touch, and pain (107). Skin consists of three main layers: an epidermis outer layer with melanocytes, a dermis second layer with nerve endings, sweat glands, sebaceous glands, and hair follicles, and a third fatty layer of subcutaneous tissues. Although the skin conditions and diseases are vast, the widely known include melanoma, acne, and hair loss.

Skin is highly accessible to optical examination by being the superficial structure. Comprising lipid-rich structures including the sebaceous glands and adipocytes, skin is a suitable target for CARS imaging. Using video-rate CARS microscopy, Evans et al. (21) described the skin composition in the ears of living mice and tracked the diffusion of topically applied baby oil into the skin. Using compound Raman microscopy, Slipchenko et al. (47) measured the lipid composition of subcutaneous adipocytes and sebaceous glands. Using CARS microscopy, Zimmerly et al. (108) measured the distribution and concentration of d-glycine in human hair. Together, these studies highlight a growing interest in the application of CARS microscopy to the studies of skin biology. It is feasible that CARS microscopy will be widely used to track the diffusion of topically applied ointments and drugs and to evaluate the effects of cosmetic, skin care, and hair care products on the texture, moisture, and lipid composition of the skin and hair.

### Study of myelin diseases

Demyelination, or the loss of the myelin sheaths around axons, is a hallmark of many neurodegenerative diseases such as leukodystrophies and multiple sclerosis (2). The loss of the myelin sheaths impairs signal conduction along axons and reduces the communication among nerve cells. Individuals with demyelinated diseases could exhibit any neurological symptom including impairments of speech, cognition, vision, and coordination. The causes of demyelinated diseases are unknown but the risk factors might include genetic, environmental, and infection (2, 109). Universally, the demyelination process involves attacks on the myelin sheaths by the immune system. Currently, there is no cure for demyelinated diseases. Existing treatments

mainly aim at inhibiting inflammation to curtail further attack on the myelin sheaths.

CARS microscopy has been applied successfully to the studies of demyelination in the past several years. The myelin membranes contain about 70% lipid by weight and the high-density  $\text{CH}_2$  groups produce a large CARS signal (110). Wang et al. (41) reported the first application of CARS microscopy to visualize the myelin sheaths, the node of Ranvier, and the Schmidt-Lanterman incisure in explanted spinal cord tissues. Fu et al. (111) characterized in real time the process of lysophosphatidylcholine-induced myelin degradation *in vitro* and *in vivo*. Huff et al. (43) described the microenvironments of the sciatic nerves in a living mouse. In another study, Fu et al. (112) examined the mechanism underlying glutamate excitotoxicity by monitoring paranodal myelin splitting and retraction (Fig. 4B). Henry et al. (113) monitored in real time demyelination and remyelination of sciatic nerves in living rats following peripheral nerve injuries. Most recently, Shi et al. (114) used CARS microscopy to evaluate the ability of copolymer micelles in repairing spinal cord injuries. Together, these studies demonstrated the versatility of CARS microscopy to the studies of myelin diseases.

CARS microscopy is uniquely advantageous for the studies of demyelination for several reasons. First, CARS imaging does not require sample processing to visualize myelin structures as in histology or electron microscopy. This advantage reduces any associated preparation time for samples. Second, CARS imaging does not require labeling for visualization; thus, it allows long-term visualization of the myelin sheaths (41, 115). Third, CARS-based multimodal microscopy allows simultaneous visualization of myelin sheaths and cellular processes during demyelination (111–113). This capability is invaluable to the studies of molecular mechanisms underlying myelin diseases. Fourth, CARS microscopy allows *in vivo* imaging of the myelin sheaths (43, 44, 113). This capability is invaluable for the investigation of the causes of myelin diseases or the evaluation of drugs aiming at curtailing further demyelination or restoring the structure and function of the myelin sheaths. Given the demonstrated advantages, it is conceivable that CARS microscopy continues to be a technique of choice for the future studies of the myelin diseases.

## DISCUSSION

CARS microscopy is a versatile instrument suitable for the studies of lipids in diseases. CARS microscopy relies on the intrinsic molecular vibration for contrast mechanism (18). Therefore, it is particularly sensitive to the lipid-rich structures due to the abundance of the  $\text{CH}_2$  group and the distinctive  $\text{CH}_2$  stretch-vibration frequency at  $2840\text{ cm}^{-1}$ . The strong signal-to-noise ratio arising from the  $\text{CH}_2$  vibration allows for short integration time and enables image acquisition with speed as high as video rate (21). Continuous applications of CARS microscopy to the studies of lipid-related diseases are shedding light on the full capability of CARS imaging. As lipid-related diseases continue

to be the leading causes of death worldwide, it is foreseeable that CARS microscopy will emerge as an indispensable tool to illuminate the roles of lipids in health and diseases.

Technically, coupling CARS microscopy with other NLO imaging modalities, such as TPEF and SHG, expands the observable biological structures and broadens the applicability of CARS microscopy to the studies of complex biological systems (116). Furthermore, the integration of spontaneous Raman spectroscopy onto the CARS microscope platform provides complete high-resolution Raman spectral information of the samples (47). Compact laser sources (38, 117, 118) are being developed to make CARS microscopy more accessible to biomedical researchers by reducing its cost, footprint, and complexity. Increasing the penetration depth with CARS endoscopy (84, 85) or miniature microscope objective (119) could allow CARS imaging from the lumen of the intestine, esophagus, and artery, or CARS imaging of lipid-rich tissues with minimally invasive surgery. Finally, though CARS microscopes described in recent literature have been home-built, turn-key commercial CARS microscopes have been recently released. The commercialization of CARS microscopy is expected to render this technology more accessible and enable its widespread applications to biomedical research. Collectively, an affordable, easy-to-operate, versatile, and multifunctional CARS microscope promises to be a powerful tool for understanding the role of lipids in health and diseases.

Finally, we discuss limitations of the technique and potential solutions. A major drawback of CARS microscopy is the existence of a nonresonant background. The CARS signal contains a Raman-shift dependent resonant contribution and a Raman-shift independent electronic contribution that could be enhanced in the presence of two-photon electronic resonance. The electronic contribution disperses the CARS spectral profile (120) and gives a vibrationally nonresonant background in CARS images. For myelin sheaths and lipid bodies, the high-density C-H vibrational oscillators produce a resonant CARS signal that is much larger than the nonresonant contribution from water and other biological structures. In these cases, the large resonant signals permit selective CARS imaging of myelin in a complex tissue environment and lipid droplets in mammalian cells, model organisms, and mice, as reviewed here. The nonresonant background, however, makes it difficult to perform CARS imaging based on the fingerprint bands. Various advanced CARS imaging techniques have been developed to suppress the nonresonant contribution, including polarization-sensitive detection (35), time-resolved detection (121), heterodyne detection (122, 123), and frequency modulation (122, 124). However, the complexity of these techniques hinders their biological applications.

The recently developed stimulated Raman scattering (SRS) microscopy (125–128) provides a simple and robust way to overcome the nonresonant background problem. The SRS signal is free of the nonresonant background via heterodyne detection of Raman-induced intensity changes

of the input laser beams. The heterodyne detection also renders the SRS signal linearly proportional of the vibrational oscillators in the focal volume, making it more sensitive for detection of low-concentration molecules. Importantly, because the SRS process occurs simultaneously with CARS, the SRS modality can be implemented on a CARS microscope with the addition of a laser intensity modulator, a photodiode detector, and a lock-in amplifier. Although a detailed description of this technique is beyond the scope of this review, two recent applications have shown great potential of SRS microscopy in high-speed vibrational imaging of samples with fingerprint Raman bands (129, 130) **■**

## REFERENCES

1. van Meer, G., D. R. Voelker, and G. W. Feigenson. 2008. Membrane lipids: where they are and how they behave. *Nat. Rev. Mol. Cell Biol.* **9**: 112–124.
2. Lazzarini, R. A. 2004. Myelin Biology and its Disorders. Elsevier Academic Press, San Diego, CA.
3. Krahmer, N., Y. Guo, R. V. Farese, Jr., and T. C. Walther. 2009. SnapShot: Lipid droplets. *Cell* **139**: 1024–1024 e1021.
4. Ogretmen, B., and Y. A. Hannun. 2004. Biologically active sphingolipids in cancer pathogenesis and treatment. *Nat. Rev. Cancer.* **4**: 604–616.
5. Wymann, M. P., and R. Schneider. 2008. Lipid signalling in disease. *Nat. Rev. Mol. Cell Biol.* **9**: 162–176.
6. Kopelman, P. G. 2000. Obesity as a medical problem. *Nature.* **404**: 635–643.
7. Despres, J. P., and I. Lemieux. 2006. Abdominal obesity and metabolic syndrome. *Nature.* **444**: 881–887.
8. Sommer, U., H. Herscovitz, F. K. Welty, and C. E. Costello. 2006. LC-MS-based method for the qualitative and quantitative analysis of complex lipid mixtures. *J. Lipid Res.* **47**: 804–814.
9. Simons, K., and D. Toomre. 2000. Lipid rafts and signal transduction. *Nat. Rev. Mol. Cell Biol.* **1**: 31–39.
10. Maier, O., V. Oberle, and D. Hoekstra. 2002. Fluorescent lipid probes: some properties and applications (a review). *Chem. Phys. Lipids.* **116**: 3–18.
11. Kuerschner, L., C. S. Ejsing, K. Ekroos, A. Shevchenko, K. I. Anderson, and C. Thiele. 2005. Polyene-lipids: a new tool to image lipids. *Nat. Methods.* **2**: 39–45.
12. Listenberger, L., and D. Brown. 2007. Fluorescent detection of lipid droplets and associated proteins. *Curr. Protoc. Cell Biol.* **35**: 24.22.21–24.22.11.
13. Baumgart, T., A. T. Hammond, P. Sengupta, S. T. Hess, D. A. Holowka, B. A. Baird, and W. W. Webb. 2007. Large-scale fluid/fluid phase separation of proteins and lipids in giant plasma membrane vesicles. *Proc. Natl. Acad. Sci. USA.* **104**: 3165–3170.
14. George, J., and J. Thomas. 1999. Raman spectroscopy of protein and nucleic acid assemblies. *Annu. Rev. Biomol. Struct.* **28**: 1–27.
15. Kneipp, K., H. Kneipp, I. Itzkan, R. R. Dasari, and M. S. Feld. 1999. Ultrasensitive chemical analysis by Raman spectroscopy. *Chem. Rev.* **99**: 2957–2976.
16. Chan, J., S. Fore, S. Wachsman-Hogiu, and T. Huser. 2008. Raman spectroscopy and microscopy of individual cells and cellular components. *Laser Photon Rev.* **2**: 325–349.
17. Krafft, C., B. Dietzek, and J. Popp. 2009. Raman and CARS microscopy of cells and tissues. *Analyst (Lond.)* **134**: 1046–1057.
18. Cheng, J. X., and X. S. Xie. 2004. Coherent anti-Stokes Raman scattering microscopy: instrumentation, theory, and applications. *J. Phys. Chem. B.* **108**: 827–840.
19. Mukamel, S. 1995. Principles of Nonlinear Optical Spectroscopy. Oxford University Press, New York.
20. Cheng, J. X., Y. K. Jia, G. F. Zheng, and X. S. Xie. 2002. Laser-scanning coherent anti-Stokes Raman scattering microscopy and applications to cell biology. *Biophys. J.* **83**: 502–509.
21. Evans, C. L., E. O. Potma, M. Puoris'haag, D. Cote, C. P. Lin, and X. S. Xie. 2005. Chemical imaging of tissue in vivo with video-rate coherent anti-Stokes Raman scattering microscopy. *Proc. Natl. Acad. Sci. USA.* **102**: 16807–16812.

22. Cheng, J. X., A. Volkmer, and X. S. Xie. 2002. Theoretical and experimental characterization of coherent anti-Stokes Raman scattering microscopy. *J. Opt. Soc. Am. B* **19**: 1363–1375.
23. Cheng, J. X. 2007. Coherent anti-Stokes Raman Scattering microscopy. *Appl. Spectrosc.* **61**: 197a–208a.
24. Muller, M., and A. Zumbusch. 2007. Coherent anti-Stokes Raman scattering microscopy. *Chem. Phys. Chem.* **8**: 2157–2170.
25. Evans, C. L., and X. S. Xie. 2008. Coherent anti-Stokes Raman scattering microscopy: chemically selective imaging for biology and medicine. *Annu. Rev. Anal. Chem.* **1**: 883–909.
26. Le, T. T., and J. X. Cheng. 2009. Non-linear optical imaging of obesity-related health risks. [Review] *J. Innov. Opt. Health Sci.* **2**: 9–25.
27. Wang, H. W., Y. Fu, T. B. Huff, T. T. Le, H. F. Wang, and J. X. Cheng. 2009. Chasing lipids in health and diseases by coherent anti-Stokes Raman scattering microscopy. *Vib. Spectrosc.* **50**: 160–167.
28. Maker, P. D., and R. W. Terhune. 1965. Study of optical effects due to an induced polarization third order in the electric field strength. *Phys. Rev.* **137**: A801–A818.
29. Begley, R. F., A. B. Harvey, and R. L. Byer. 1974. Coherent anti-Stokes Raman spectroscopy. *Appl. Phys. Lett.* **25**: 387–390.
30. Lenson, M. D., and S. S. Kano. 1988. Introduction to Nonlinear Laser Spectroscopy. Academic Press, San Diego.
31. Duncan, M. D., J. Reintjes, and T. J. Manuccia. 1982. Scanning coherent anti-Stokes Raman microscope. *Opt. Lett.* **7**: 350–352.
32. Zumbusch, A., G. R. Holtom, and X. S. Xie. 1999. Three-dimensional vibrational imaging by coherent anti-Stokes Raman scattering. *Phys. Rev. Lett.* **82**: 4142–4145.
33. Fu, Y., H. F. Wang, R. Y. Shi, and J. X. Cheng. 2006. Characterization of photodamage in coherent anti-Stokes Raman scattering microscopy. *Opt. Express.* **14**: 3942–3951.
34. Ganikhanov, F., S. Carrasco, X. S. Xie, M. Katz, W. Seitz, and D. Kopf. 2006. Broadly tunable dual-wavelength light source for coherent anti-Stokes Raman scattering microscopy. *Opt. Lett.* **31**: 1292–1294.
35. Cheng, J. X., L. D. Book, and X. S. Xie. 2001. Polarization coherent anti-Stokes Raman scattering microscopy. *Opt. Lett.* **26**: 1341–1343.
36. Hashimoto, M., T. Araki, and S. Kawata. 2000. Molecular vibration imaging in the fingerprint region by use of coherent anti-Stokes Raman scattering microscopy with a collinear configuration. *Opt. Lett.* **25**: 1768–1770.
37. Tang, S., T. B. Krasieva, Z. Chen, G. Tempea, and B. J. Tromberg. 2006. Effect of pulse duration on two-photon excited fluorescence and second harmonic generation in nonlinear optical microscopy. *J. Biomed. Opt.* **11**: 020501–020503.
38. Pegoraro, A. F., A. Ridsdale, D. J. Moffatt, J. P. Pezacki, B. K. Thomas, L. B. Fu, L. Dong, M. E. Fermann, and A. Stolow. 2009. All-fiber CARS microscopy of live cells. *Opt. Express.* **17**: 20700–20706.
39. Chen, H., H. Wang, M. N. Slipchenko, Y. Jung, Y. Shi, J. Zhu, K. K. Buhman, and J. X. Cheng. 2009. A multimodal platform for nonlinear optical microscopy and microspectroscopy. *Opt. Express.* **17**: 1282–1290.
40. Nan, X. L., J. X. Cheng, and X. S. Xie. 2003. Vibrational imaging of lipid droplets in live fibroblast cells with coherent anti-Stokes Raman scattering microscopy. *J. Lipid Res.* **44**: 2202–2208.
41. Wang, H. F., Y. Fu, P. Zickmund, R. Y. Shi, and J. X. Cheng. 2005. Coherent anti-Stokes Raman scattering imaging of axonal myelin in live spinal tissues. *Biophys. J.* **89**: 581–591.
42. Volkmer, A., J. X. Cheng, and X. S. Xie. 2001. Vibrational imaging with high sensitivity via epidetected coherent anti-Stokes Raman scattering microscopy. *Phys. Rev. Lett.* **87**: 23901.
43. Huff, T. B., and J. X. Cheng. 2007. In vivo coherent anti-Stokes Raman scattering imaging of sciatic nerve tissue. *J. Microsc.* **225**: 175–182.
44. Fu, Y., T. B. Huff, H. W. Wang, H. F. Wang, and J. X. Cheng. 2008. *Ex vivo* and *in vivo* imaging of myelin fibers in mouse brain by coherent anti-Stokes Raman microscopy. *Opt. Express.* **16**: 19396–19409.
45. Fu, Y., H. F. Wang, R. Y. Shi, and J. X. Cheng. 2007. Second harmonic and sum frequency generation imaging of fibrous astroglial filaments in ex vivo spinal tissues. *Biophys. J.* **92**: 3251–3259.
46. Moreaux, L., O. Sandro, S. Charpak, M. Blanchard-Desce, and J. Mertz. 2001. Coherent scattering in multi-harmonic light microscopy. *Biophys. J.* **80**: 1568–1574.
47. Slipchenko, M. N., T. T. Le, H. T. Chen, and J. X. Cheng. 2009. High-speed vibrational imaging and spectral analysis of lipid bodies by compound Raman microscopy. *J. Phys. Chem. B* **113**: 7681–7686.
48. Le, T. T., H. M. Duren, M. N. Slipchenko, C. D. Hu, and J. X. Cheng. 2010. Label-free quantitative analysis of lipid metabolism in living *Caenorhabditis elegans*. *J. Lipid Res.* **51**: 672–677.
49. Martin, S., and R. G. Parton. 2006. Lipid droplets: a unified view of a dynamic organelle. *Nat. Rev. Mol. Cell Biol.* **7**: 373–378.
50. Farese, R. V., Jr., and T. C. Walther. 2009. Lipid droplets finally get a little R-E-S-P-E-C-T. *Cell* **139**: 855–860.
51. Murphy, D. J. 2001. The biogenesis and functions of lipid bodies in animals, plants and microorganisms. *Prog. Lipid Res.* **40**: 325–438.
52. Listenberger, L. L., X. L. Han, S. E. Lewis, S. Cases, R. V. Farese, D. S. Ory, and J. E. Schaffer. 2003. Triglyceride accumulation protects against fatty acid-induced lipotoxicity. *Proc. Natl. Acad. Sci. USA* **100**: 3077–3082.
53. Holthuis, J. C., and T. P. Levine. 2005. Lipid traffic: floppy drives and a superhighway. *Nat. Rev. Mol. Cell Biol.* **6**: 209–220.
54. Miyanari, Y., K. Atsuzawa, N. Usuda, K. Watashi, T. Hishiki, M. Zayas, R. Bartenschlager, T. Wakita, M. Hijikata, and K. Shimotohno. 2007. The lipid droplet is an important organelle for hepatitis C virus production. *Nat. Cell Biol.* **9**: 1089–1097.
55. Brasaemle, D. L. 2007. Thematic review series: adipocyte biology. The perilipin family of structural lipid droplet proteins: stabilization of lipid droplets and control of lipolysis. *J. Lipid Res.* **48**: 2547–2559.
56. Miura, S., J. W. Gan, J. Brzostowski, M. J. Parisi, C. J. Schultz, C. Lontos, B. Oliver, and A. R. Kimmel. 2002. Functional conservation for lipid storage droplet association among Perilipin, ADRP, and TIP47 (PAT)-related proteins in mammals, *Drosophila*, and *Dictyostelium*. *J. Biol. Chem.* **277**: 32253–32257.
57. Nan, X. L., E. O. Potma, and X. S. Xie. 2006. Nonperturbative chemical imaging of organelle transport in living cells with coherent anti-stokes Raman scattering microscopy. *Biophys. J.* **91**: 728–735.
58. Yamaguchi, T., N. Omatsu, E. Morimoto, H. Nakashima, K. Ueno, T. Tanaka, K. Satouchi, F. Hirose, and T. Osumi. 2007. CGI-58 facilitates lipolysis on lipid droplets but is not involved in the vesiculation of lipid droplets caused by hormonal stimulation. *J. Lipid Res.* **48**: 1078–1089.
59. Le, T. T., and J. X. Cheng. 2009. Single-cell profiling reveals the origin of phenotypic variability in adipogenesis. *PLoS ONE* **4**: e5189.
60. Lyn, R. K., D. C. Kennedy, S. M. Sagan, D. R. Blais, Y. Rouleau, A. F. Pegoraro, X. S. Xie, A. Stolow, and J. P. Pezacki. 2009. Direct imaging of the disruption of hepatitis C virus replication complexes by inhibitors of lipid metabolism. *Virology* **394**: 130–142.
61. Kaletta, T., and M. O. Hengartner. 2006. Finding function in novel targets: *C. elegans* as a model organism. *Nat. Rev. Drug Discov.* **5**: 387–398.
62. Ashrafi, K. 2007. Obesity and the regulation of fat metabolism. In *WormBook*, ed. The *C. elegans* Research Community, WormBook.
63. Elle, I. C., L. C. B. Olsen, D. Pultz, S. V. Rodkaer, and N. J. Faergeman. 2010. Something worth dyeing for: molecular tools for the dissection of lipid metabolism in *Caenorhabditis elegans*. *FEBS Lett.* **584**: 2183–2193.
64. Mullaney, B. C., and K. Ashrafi. 2009. *C. elegans* fat storage and metabolic regulation. *Biochim. Biophys. Acta.* **1791**: 474–478.
65. McKay, R. M., J. P. McKay, L. Avery, and J. M. Graff. 2003. *C. elegans*: a model for exploring the genetics of fat storage. *Dev. Cell* **4**: 131–142.
66. Brooks, K. K., B. Liang, and J. L. Watts. 2009. The influence of bacterial diet on fat storage in *C. elegans*. *PLoS ONE* **4**: e7545.
67. Hellerer, T., C. Axang, C. Brackmann, P. Hillert, M. Pilon, and A. Enejder. 2007. Monitoring of lipid storage in *Caenorhabditis elegans* using coherent anti-Stokes Raman scattering (CARS) microscopy. *Proc. Natl. Acad. Sci. USA* **104**: 14658–14663.
68. Clokey, G. V., and L. A. Jacobson. 1986. The autofluorescent “lipofuscin granules” in the intestinal cells of *Caenorhabditis elegans* are secondary lysosomes. *Mech. Ageing Dev.* **35**: 79–94.
69. Hosokawa, H., N. Ishii, H. Ishida, K. Ichimori, H. Nakazawa, and K. Suzuki. 1994. Rapid accumulation of fluorescent material with aging in an oxygen-sensitive mutant mev-1 of *Caenorhabditis elegans*. *Mech. Ageing Dev.* **74**: 161–170.

70. Watts, J. L., and J. Browse. 2002. Genetic dissection of polyunsaturated fatty acid synthesis in *Caenorhabditis elegans*. *Proc. Natl. Acad. Sci. USA*. **99**: 5854–5859.
71. Morck, C., L. Olsen, C. Kurth, A. Persson, N. J. Storm, E. Svensson, J. O. Jansson, M. Hellqvist, A. Enejder, N. J. Faergeman, et al. 2009. Statins inhibit protein lipidation and induce the unfolded protein response in the non-sterol producing nematode *Caenorhabditis elegans*. *Proc. Natl. Acad. Sci. USA*. **106**: 18285–18290.
72. O'Rourke, E. J., A. A. Soukas, C. E. Carr, and G. Ruvkun. 2009. *C. elegans* major fats are stored in vesicles distinct from lysosome-related organelles. *Cell Metab.* **10**: 430–435.
73. Dupuy, D., N. Bertin, C. A. Hidalgo, K. Venkatesan, D. Tu, D. Lee, J. Rosenberg, N. Svrzikapa, A. Blanc, A. Carnec, et al. 2007. Genome-scale analysis of in vivo spatiotemporal promoter activity in *Caenorhabditis elegans*. *Nat. Biotechnol.* **25**: 663–668.
74. Chung, K. H., M. M. Crane, and H. Lu. 2008. Automated on-chip rapid microscopy, phenotyping and sorting of *C. elegans*. *Nat. Methods*. **5**: 637–643.
75. Choudhury, R. P., V. Fuster, and Z. A. Fayad. 2004. Molecular, cellular and functional imaging of atherothrombosis. *Nat. Rev. Drug Discov.* **3**: 913–925.
76. Fischer, A., D. E. Gutstein, Z. A. Fayad, and V. Fuster. 2000. Predicting plaque rupture: enhancing diagnosis and clinical decision-making in coronary artery disease. *Vasc. Med.* **5**: 163–172.
77. Naghavi, M., P. Libby, E. Falk, S. W. Casscells, S. Litovsky, J. Rumberger, J. J. Badimon, C. Stefanadis, P. Moreno, G. Pasterkamp, et al. 2003. From vulnerable plaque to vulnerable patient: a call for new definitions and risk assessment strategies: Part I. *Circulation*. **108**: 1664–1672.
78. Le, T. T., I. M. Langohr, M. J. Locker, M. Sturek, and J. X. Cheng. 2007. Label-free molecular imaging of atherosclerotic lesions using multimodal nonlinear optical microscopy. *J. Biomed. Opt.* **12**: 054007.
79. Wang, H. W., T. T. Le, and J. X. Cheng. 2008. Label-free imaging of arterial cells and extracellular matrix using a multimodal CARS microscope. *Opt. Commun.* **281**: 1813–1822.
80. Wang, H. W., I. M. Langohr, M. Sturek, and J. X. Cheng. 2009. Imaging and quantitative analysis of atherosclerotic lesions by CARS-based multimodal nonlinear optical microscopy. *Arterioscler. Thromb. Vasc. Biol.* **29**: 1342–1348.
81. Lim, R. S., A. Kratzer, N. P. Barry, S. Miyazaki-Anzai, M. Miyazaki, W. W. Mantulin, M. Levi, E. O. Potma, and B. J. Tromberg. 2010. Multimodal CARS microscopy determination of the impact of diet on macrophage infiltration and lipid accumulation on plaque formation in ApoE-deficient mice. *J. Lipid Res.* In press.
82. Kim, S. H., E. S. Lee, J. Y. Lee, E. S. Lee, B. S. Lee, J. E. Park, and D. W. Moon. 2010. Multiplex coherent anti-Stokes Raman spectroscopy images intact atheromatous lesions and concomitantly identifies distinct chemical profiles of atherosclerotic lipids. *Circ. Res.* **106**: 1332–1341.
83. Ko, A. C. T., A. Ridsdale, M. S. D. Smith, L. B. Mostaçõ-Guidolin, M. D. Hewko, A. F. Pegoraro, E. K. Kohlenberg, B. Schattka, M. Shiomi, A. Stolow, et al. 2010. Multimodal nonlinear optical imaging of atherosclerotic plaque development in myocardial infarction-prone rabbits. *J. Biomed. Opt.* **15**: 020501.
84. Legare, F., C. L. Evans, F. Ganikhanov, and X. S. Xie. 2006. Towards CARS endoscopy. *Opt. Express*. **14**: 4427–4432.
85. Balu, M., G. Liu, Z. Chen, B. J. Tromberg, and E. O. Potma. 2010. Fiber delivered probe for efficient CARS imaging of tissues. *Opt. Express*. **18**: 2380–2388.
86. Llewellyn, M. E., R. P. J. Barretto, S. L. Delp, and M. J. Schnitzer. 2008. Minimally invasive high-speed imaging of sarcomere contractile dynamics in mice and humans. *Nature*. **454**: 784–788.
87. DeMaria, E. J. 2007. Bariatric surgery for morbid obesity. *N. Engl. J. Med.* **356**: 2176–2183.
88. Rodriguez, L., E. Reyes, P. Fagalde, M. S. Oltra, J. Saba, C. G. Aylwin, C. Prieto, A. Ramos, M. Galvao, K. S. Gersin, et al. 2009. Pilot clinical study of an endoscopic, removable duodenal-jejunal bypass liner for the treatment of type 2 diabetes. *Diabetes Technol. Ther.* **11**: 725–732.
89. Iqbal, J., and M. M. Hussain. 2009. Intestinal lipid absorption. *Am. J. Physiol. Endocrinol. Metab.* **296**: E1183–E1194.
90. Zhu, J., B. Lee, K. K. Buhman, and J. X. Cheng. 2009. A dynamic, cytoplasmic triacylglycerol pool in enterocytes revealed by ex vivo and in vivo coherent anti-Stokes Raman scattering imaging. *J. Lipid Res.* **50**: 1080–1089.
91. Chen, H. C., and R. V. Farese, Jr. 2005. Inhibition of triglyceride synthesis as a treatment strategy for obesity: lessons from DGAT1-deficient mice. *Arterioscler. Thromb. Vasc. Biol.* **25**: 482–486.
92. Lee, B., A. M. Fast, J. Zhu, J. X. Cheng, and K. K. Buhman. 2010. Intestine specific expression of acyl CoA:diacylglycerol acyltransferase 1 (DGAT1) reverses resistance to diet-induced hepatic steatosis and obesity in *Dgat1*<sup>-/-</sup> mice. *J. Lipid Res.* In press.
93. Ramos, C. V., and H. B. Taylor. 1973. Lipid-rich carcinoma of the breast: a clinicopathologic analysis of 13 examples. *Cancer*. **33**: 812–819.
94. Sijens, P. E., P. C. Levendag, C. J. Vecht, P. vanDijk, and M. Oudkerk. 1996. H-1 MR spectroscopy detection of lipids and lactate in metastatic brain tumors. *NMR Biomed.* **9**: 65–71.
95. Rosen, P. P. 2008. *Rosen's Breast Pathology*. 3rd ed. Lippincott Williams & Wilkins, New York.
96. Menendez, J. A., and R. Lupu. 2007. Fatty acid synthase and the lipogenic phenotype in cancer pathogenesis. *Nat. Rev. Cancer*. **7**: 763–777.
97. Migita, T., S. Ruiz, A. Fornari, M. Fiorentino, C. Priolo, G. Zadra, F. Inazuka, C. Grisanzio, E. Palescandolo, E. Shin, et al. 2009. Fatty acid synthase: a metabolic enzyme and candidate oncogene in prostate cancer. *J. Natl. Cancer Inst.* **101**: 519–532.
98. Le, T. T., T. B. Huff, and J. X. Cheng. 2009. Coherent anti-Stokes Raman scattering imaging of lipids in cancer metastasis. *BMC Cancer*. **9**: 42.
99. Wang, H. W., N. Bao, T. T. Le, C. Lu, and J. X. Cheng. 2008. Microfluidic CARS cytometry. *Opt. Express*. **16**: 5782–5789.
100. Bao, N., T. T. Le, J. X. Cheng, and C. Lu. 2010. Microfluidic electroporation of tumor and blood cells: observation of nucleus expansion and implications on selective analysis and purging of circulating tumor cells. *Integr. Biol.* **2**: 113–120.
101. Le, T. T., C. W. Rehrer, T. B. Huff, M. B. Nichols, I. G. Camarillo, and J. X. Cheng. 2007. Nonlinear optical imaging to evaluate the impact of obesity on mammary gland and tumor stroma. *Mol. Imaging*. **6**: 205–211.
102. Iyengar, P., T. P. Combs, S. J. Shah, V. Gouon-Evans, J. W. Pollard, C. Albanese, L. Flanagan, M. P. Tenniswood, C. Guha, M. P. Lisanti, et al. 2003. Adipocyte-secreted factors synergistically promote mammary tumorigenesis through induction of anti-apoptotic transcriptional programs and proto-oncogene stabilization. *Oncogene*. **22**: 6408–6423.
103. Sternlicht, M. D., and Z. Werb. 2001. How matrix metalloproteinases regulate cell behavior. *Annu. Rev. Cell Dev. Biol.* **17**: 463–516.
104. Rowe, R. G., and S. J. Weiss. 2009. Navigating ECM barriers at the invasive front: the cancer cell-stroma interface. *Annu. Rev. Cell Dev. Biol.* **25**: 567–595.
105. Hsu, P. P., and D. M. Sabatini. 2008. Cancer cell metabolism: Warburg and beyond. *Cell*. **134**: 703–707.
106. Vander Heiden, M. G., L. C. Cantley, and C. B. Thompson. 2009. Understanding the Warburg effect: the metabolic requirements of cell proliferation. *Science*. **324**: 1029–1033.
107. Lumpkin, E. A., and M. J. Caterina. 2007. Mechanisms of sensory transduction in the skin. *Nature*. **445**: 858–865.
108. Zimmerley, M., C. Y. Lin, D. C. Oertel, J. M. Marsh, J. L. Ward, and E. O. Potma. 2009. Quantitative detection of chemical compounds in human hair with coherent anti-Stokes Raman scattering microscopy. *J. Biomed. Opt.* **14**: 044019.
109. Waxman, S. G. 1998. Demyelinating diseases - new pathological insights, new therapeutic targets. *N. Engl. J. Med.* **338**: 323–325.
110. Siegel, G. J., B. W. Agranoff, R. W. Alberts, and P. B. Molinoff. 1994. *Basic Neurochemistry: Molecular, Cellular, and Medical Aspects*. Raven Press Ltd., New York.
111. Fu, Y., H. F. Wang, T. B. Huff, R. Shi, and J. X. Cheng. 2007. Coherent anti-stokes Raman scattering imaging of myelin degradation reveals a calcium-dependent pathway in lyso-PtdCho-induced demyelination. *J. Neurosci. Res.* **85**: 2870–2881.
112. Fu, Y., W. Sun, Y. Shi, R. Shi, and J. X. Cheng. 2009. Glutamate excitotoxicity inflicts paranodal myelin splitting and retraction. *PLoS ONE*. **4**: e6705.
113. Henry, F. P., D. Cote, M. A. Randolph, E. A. Z. Rust, R. W. Redmond, I. E. Kochevar, C. P. Lin, and J. M. Winograd. 2009. real-time in vivo assessment of the nerve microenvironment with coherent anti-Stokes Raman scattering microscopy. *Plast. Reconstr. Surg.* **123**: 123s–130s.
114. Shi, Y., S. Kim, T. B. Huff, R. B. Borgens, K. Park, R. Shi, and J. X. Cheng. 2010. Effective repair of traumatically injured spinal

- cord by nanoscale block copolymer micelles. *Nat. Nanotechnol.* **5**: 80–87.
115. Belanger, E., S. Begin, S. Laffray, Y. De Koninck, R. Vallee, and D. Cote. 2009. Quantitative myelin imaging with coherent anti-Stokes Raman scattering microscopy: alleviating the excitation polarization dependence with circularly polarized laser beams. *Opt. Express.* **17**: 18419–18432.
116. Huff, T. B., Y. Shi, Y. Fu, H. Wang, and J. X. Cheng. 2008. Multimodal nonlinear optical microscopy and applications to central nervous system imaging. *IEEE J. Sel. Top. Quantum Electron.* **14**: 4–9.
117. Krauss, G., T. Hanke, A. Sell, D. Träutlein, A. Leitenstorfer, R. Selm, M. Winterhalder, and A. Zumbusch. 2009. Compact coherent anti-Stokes Raman scattering microscope based on a picosecond two-color Er: fiber laser system. *Opt. Lett.* **34**: 2847–2849.
118. Kieu, K., B. G. Saar, G. R. Holtom, X. S. Xie, and F. W. Wise. 2009. High-power picosecond fiber source for coherent Raman microscopy. *Opt. Lett.* **34**: 2051–2053.
119. Wang, H., T. B. Huff, Y. Fu, K. Y. Jia, and J. X. Cheng. 2007. Increasing the imaging depth of coherent anti-Stokes Raman scattering microscopy with a miniature microscope objective. *Opt. Lett.* **32**: 2212–2214.
120. Shen, Y. R. 1984. *The Principles of Nonlinear Optics*. John Wiley and Sons Inc., New York.
121. Volkmer, A., L. D. Book, and X. S. Xie. 2002. Time-resolved coherent anti-Stokes Raman scattering microscopy: imaging based on Raman free induction decay. *Appl. Phys. Lett.* **80**: 1505–1507.
122. Jurna, M., J. P. Korterik, C. Otto, J. L. Herek, and H. L. Offerhaus. 2008. Background free CARS imaging by phase sensitive heterodyne CARS. *Opt. Express.* **16**: 15863–15869.
123. Potma, E. O., C. L. Evans, and X. S. Xie. 2006. Heterodyne coherent anti-Stokes Raman scattering (CARS) imaging. *Opt. Lett.* **31**: 241–243.
124. Ganikhanov, F., C. L. Evans, B. G. Saar, and X. S. Xie. 2006. High-sensitivity vibrational imaging with frequency modulation coherent anti-Stokes Raman scattering (FM CARS) microscopy. *Opt. Lett.* **31**: 1872–1874.
125. Ploetz, E., S. Laimgruber, S. Berner, W. Zinth, and P. Gilch. 2007. Femtosecond stimulated Raman microscopy. *Appl. Phys. B.* **87**: 389–393.
126. Freudiger, C. W., W. Min, B. G. Saar, S. Lu, G. R. Holtom, C. W. He, J. C. Tsai, J. X. Kang, and X. S. Xie. 2008. Label-free biomedical imaging with high sensitivity by stimulated Raman scattering microscopy. *Science.* **322**: 1857–1861.
127. Ozeki, Y., F. Dake, S. i. Kajiyama, K. Fukui, and K. Itoh. 2009. Analysis and experimental assessment of the sensitivity of stimulated Raman scattering microscopy. *Opt. Express.* **17**: 3651–3658.
128. Nandakumar, P., A. Kovalev, and A. Volkmer. 2009. Vibrational imaging based on stimulated Raman scattering microscopy. *N. J. Phys.* **11**: 033026.
129. Slipchenko, M. N., H. Chen, D. R. Ely, Y. Jung, M. T. Carvajal, and J-X. Cheng. 2010. Vibrational imaging of tablets by epidected stimulated Raman scattering microscopy. *Analyst (Lond.)*. 10.1039/C0AN00252F.
130. Saar, B. G., Y. Zeng, C. W. Freudiger, Y-S. Liu, M. E. Himmel, X. S. Xie, and S-Y. Ding. 2010. Label-free, real-time monitoring of biomass processing with stimulated Raman scattering microscopy. *Angew. Chem. Int. Ed.* **49**: 10.1002/anie.201000900.